



Role of entrainment in the stabilisation of jet-in-hot-coflow flames

E. Oldenhof*, M.J. Tummers, E.H. van Veen, D.J.E.M. Roekaerts

Department of Multi-Scale Physics, Delft University of Technology, Lorentzweg 1, 2628 CJ Delft, The Netherlands

ARTICLE INFO

Article history:

Received 8 July 2010

Received in revised form 16 November 2010

Accepted 14 December 2010

Available online 21 January 2011

Keywords:

Autoignition

Flameless combustion

MILD combustion

Jet-in-hot-coflow

Entrainment

Favre average

ABSTRACT

The aim of the research on the Delft jet-in-hot coflow (DJHC) burner is to gain understanding in the interplay of turbulence and chemistry in conditions as encountered in devices operating in flameless combustion mode, and to test the validity of numerical models when applied to these flameless combustion conditions. Datasets on velocities, temperatures and qualitative OH data of several Dutch natural gas flames in the DJHC burner have been obtained and are discussed in this paper. It was found that the mean velocity and turbulent stresses are not significantly affected by the chemical reactions, which is in line with the very moderate increase of mean temperatures in the flames. Even at heights where flame structures are present, peak temperatures do not always approach the adiabatic flame temperature. With both flame luminescence and OH-PLIF measurements, it is seen that chemical reactions begin to occur at a lower location when the jet velocity (and thereby the jet Reynolds number) is increased. By analysing the velocity and temperature data in the near-nozzle region, the entrainment of coflow fluid into the turbulent jet has been quantified. The increased entrainment of the higher Reynolds number jet, in combination with the positive temperature gradient in radial direction in the near field of the jet, is shown to be responsible for the decrease of the height where reactions start to occur.

© 2010 The Combustion Institute. Published by Elsevier Inc. All rights reserved.

1. Introduction

By operating furnaces and boilers [1] and also gas turbines [2] in flameless (or MILD) combustion mode, high efficiencies can be combined with very low NO_x emissions. Flameless combustion therefore offers attractive characteristics, from both an environmental and an economic point of view, even more so in the light of the increasingly strict regulations on CO_2 and NO_x [3] emissions. However, large scale implementation of this technique is hampered by the risks associated with adopting a relatively unknown new technique.

The ability to predict (turbulent) flames by computer models can speed up the development and implementation of more advanced combustion techniques [4]. A general insight in the specific demands of numerical models to accurately predict the characteristics (for instance, heat fluxes and emissions) of flameless combustion would therefore be beneficial to its implementation. Several computational studies have been carried out on (semi)-industrial-scale setups operating in flameless mode [5–8]. However, dealing with the complex turbulence–chemistry interaction in this combustion mode accurately and computationally efficiently remains a challenge. Moreover, the reasons for success or failure of particular models are still unclear. This is, at least partially, caused by the limited (optical) access provided by these

setups, hindering detailed studies on for instance the statistics of the turbulent flow and temperature field throughout the domain. As a result, there are not many quantities to be used for validation. Given the large number of physical processes occurring in a furnace environment, this makes the isolation and investigation of a single aspect troublesome.

To study the interplay of turbulence and chemistry in more detail, it is therefore advantageous to simplify the geometry, while retaining the physical processes of interest, and to make the setup optically accessible. Research on such prototypical laboratory-scale flames with the level of detail offered by modern laser-diagnostics has resulted in progress in the area of turbulent combustion, by providing data for model-validation and/or by the information contained in the experimental data itself [4,9].

In this light, studying flameless combustion in an open, unconfined setup might give valuable insights, provided that the circumstances resemble those found locally in a furnace. Several laboratory scale jet flames with a vitiated coflow have been developed, most notably the Cabra et al. burner [10], and the Adelaide burner [11].

The Cabra burner was designed to capture the features of recirculation burners. Its most striking feature is the large diameter of its coflow, providing homogeneous boundary conditions over a large range, such that it can be considered a two-stream problem. This burner was not aimed specifically at investigating flameless combustion, and it might be argued that the oxygen mole fraction in the coflow (X_{O_2} of 0.15 or 0.12, for the $\text{H}_2\text{--N}_2$ and CH_4/air jet flames respectively [12]) is rather high for that purpose. Multiple

* Corresponding author. Fax: +31 15 27 81204.

E-mail address: E.Oldenhof@tudelft.nl (E. Oldenhof).

detailed measurement campaigns have been carried out, providing a comprehensive dataset of single-point scalar statistics [13,14] and information on velocities [15]. Furthermore, joint temperature, OH, and H_2CO measurements have been performed [16].

The Adelaide burner was designed to study flameless combustion, with low oxygen mass fractions in the coflow (typically 3–9%) and a small temperature increase in the reaction zone as a result. Detailed species measurements [11] and also joint temperature, OH, and H_2CO measurements [17] on flames with $\text{CH}_4\text{--H}_2$ in the fuel jet have been carried out.

In this paper the detailed results of temperature and velocity measurements in the Delft jet-in-hot coflow burner are reported, for three different coflow cases (different temperatures and oxygen mass fractions) and jet Reynolds numbers ranging from 2500 to 8800. The results are analysed with the previous findings on the flame stabilisation in mind, namely, the flame is stabilised by randomly formed autoignition spots that grow while being convected downstream by the mean flow [18]. Datasets of the various flames, containing information on velocities, temperatures, OH-fields and the coflow-composition are available upon request.

2. Experimental setup

2.1. DJHC-burner

The design of the Delft jet-in-hot coflow (DJHC) burner is based on that of the Adelaide jet-in-hot coflow burner. The main difference is that the latter uses addition of N_2 to cool down the coflow whereas the DJHC burner uses cooling of the coflow through radiative and convective heat losses along the burner pipe. Another difference is found in the design of the secondary burner, which allows for the addition of seeding particles in the DJHC-burner, to act as tracers in for instance LDA or PIV measurements. The schematic of the burner is shown in Fig. 1. The secondary burner, which generates the hot coflow, is a ring-burner. Its design was found to yield an axi-symmetric flame, and it is operated in partially premixed mode (by adding 24 nl/min of air to the fuel

stream) to help it stabilise. The secondary burner creates a flame with a length of about 0.4 m. A grid is located 0.11 m upstream of the burner exit plane, to keep the fuel pipe centered and to help the coflow lose heat. The outer burner tube radiates most strongly at the height of the distribution grid, indicating that this cooling mechanism is effective. The central fuel pipe (with internal diameter 4.5 mm) is cooled by constantly flushing air through the concentric cooling air ducts, thus preventing excessive heating of the main fuel jet. The main flow of air passes through the air inlets at the bottom and it is this flow that carries the seeding particles. A z,r -coordinate system is used centered on the exit of the fuel pipe. The velocities corresponding to these directions are u and v , respectively.

2.2. LDA system

LDA measurements were performed with a two-component, dual beam TSI-system. The green line (514.5 nm) and blue line (488 nm) of a 10 W Continuum Argon-ion laser were used to measure the axial and radial velocity components directly. Two of the incident beams (one of each color) were frequency pre-shifted over 40 MHz by a Bragg cell to enable the detection of instantaneous flow reversals and stagnant flow. The focusing lens had a 82 mm aperture and a focal length of 250 mm. The length and diameter of the measurement volume were 1.7 mm and 0.12 mm, respectively. The fringe distances for the green and blue channel were 2.6 μm and 2.5 μm . Alumina (Al_2O_3) particles with an average size of about 1 μm were used as seeding particles. Two cyclone-type particle generators were used to seed the air and fuel separately. The generators have a provision that enables the control of the seed density in both the coflow and in the fuel jet. This provision was used to equalise the seeding density in the both flows, thereby minimizing errors related to so-called conditional seeding. The data rate (number of bursts per second) was used as an indicator, as it is proportional to the fluid density, the velocity magnitude and the seeding density. This proportionality was therefore used to equalize the seeding densities: the ratio of the data rates of the unmixed fuel- and coflow streams was made approximately equal to the ratio of their products of axial velocity and fluid density. The light scattered by the seeding particles was collected in back-scatter mode. The photomultiplier output signals were electronically down-mixed, and subsequently fed to a FSA-3000 signal processor to determine the instantaneous velocity of light-scattering particles. All statistics were computed as transit-time weighted results to eliminate the effects of the velocity bias. Autocorrelation functions of the axial velocity component were constructed from time series with 4×10^5 velocity samples that were acquired at a mean data rate of approximately 500 Hz by using the slotting method with local normalisation [19].

2.3. CARS system

Temperatures were determined with a CARS system that has been described in detail elsewhere [20]. It is based on an injection-seeded, frequency-doubled Nd:YAG laser (Spectron SL805 SLM), which yields 500 mJ per pulse at 532 nm with a pulse duration of 12 ns at 10 Hz repetition rate. About 80% of the radiation is used to pump a modeless Stokes dye laser (Mode-X ML-3), emitting a broadband profile around 607 nm for Rhodamine 640 in methanol. The remaining 20% of the pump laser travels along a delay line and is split into two beams with equal intensity. The Stokes beam and the two beams at 532 nm are focused by an aplanat lens with a focal length of 300 mm in a planar-boxcars phase-matching configuration. With this configuration, a CARS probe volume of 700 μm length and 35 μm diameter is obtained. The generated CARS radiation is recollimated and combined with an attenuated

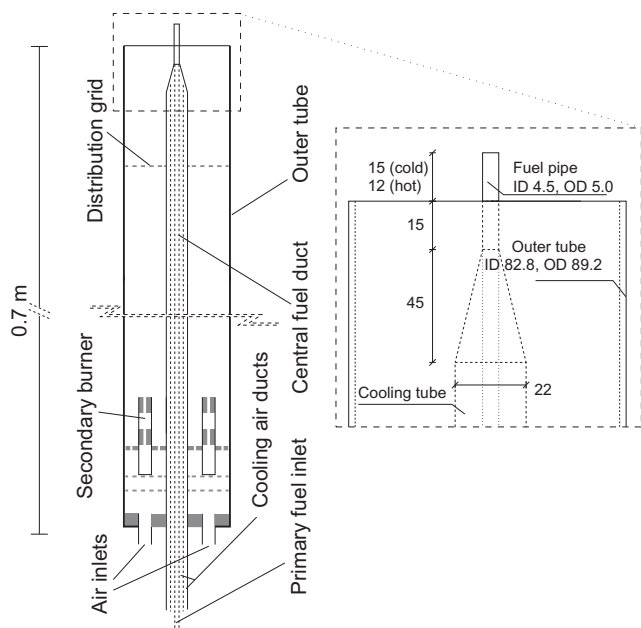


Fig. 1. Schematic design of the Delft JHC burner, with relevant dimensions in the inset. Two dimensions are given for the vertical extent of the fuel tube above the outer tube, for the cold situation and the hot situation. The difference is due to the uneven thermal expansion of the fuel- and outer tube.

sample of the Stokes beam on a dichroic beam splitter. The beams are focused onto the entrance of an echelle spectrometer, and their spectra are dispersed on a CCD detector with 1100×330 pixels. The spectra are contained in two strips of 1100 intensity values, which are digitized by an 18-bit AD converter and stored. With Dacapo software [20] the CARS spectrum is referenced to the simultaneously measured Stokes excitation profile and fitted to a library of theoretical, temperature-dependent spectra. The single-shot imprecision of the system is 1–4% over a range from 2000 K to 300 K. The inaccuracy is estimated to be 20 K. For each point in space, mean temperatures were determined from the results of 1000 single-shot CARS spectra.

2.4. OH-PLIF imaging system

A frequency-doubled, pulsed Nd:YAG laser (Spectra Physics PRO250-10) pumped a Syrah PrecisionScan dye laser using Rhodamine 590 in methanol. The second harmonic radiation from the dye laser was used to excite the $Q_1(6)$ line of the $A^2\Sigma^+ - X^2\Pi$ (1,0) transition at 282.927 nm. The UV energy was measured to be about 10 mJ/pulse. Three cylindrical lenses transformed the laser beam into a sheet with a height of approximately 80 mm and an approximate thickness of 200 μm . Fluorescence from the $A^2\Sigma^+ - X^2\Pi$ (0,0) and 1,1) transitions at 305–315 nm was collected through a Semrock narrowband filter and a UV-Nikkor 105 mm $f/4.5$ lens. The images were recorded by an intensified high-speed camera (Lambert Instruments HI-CAM CR) operating at the full resolution of 1280×1024 pixels. A mean off-resonance image was subtracted from the images to determine the mean fluorescence signal. Given a certain point in the flame, the mean OH fluorescence signal depends on the laser sheet intensity and the sensitivity of the camera. This aspect was investigated by traversing the flame vertically through the light-sheet keeping the camera position constant and determining the mean signal strength. It was found that the resulting mean signal strength for a given point in the flame (flame DJHC-I, at $z \approx 90$ mm) is within 30% of the value in the center of the light sheet over a height of 55 mm, which is considered acceptable for the purpose of flame visualisation. To obtain statistics of sufficient quality, 1000 images were recorded for each flame.

2.5. Flue gas measurements

Oxygen measurements were performed with a Testo 335 flue-gas analyser, with a specified inaccuracy of $\pm 0.20\%$. The measured oxygen volume fractions in the coflow were converted to mass fractions using the results from equilibrium chemistry calculations with the species of the detailed Warnatz-mechanism that includes C-2 chemistry (see [21], pp. 333–339).

3. Case description

Three different settings of the secondary burner, affecting mainly the coflow temperature, were used. The resulting coflow

properties are summarised in Table 1. The coflow properties (velocity, temperature and oxygen mass fraction) vary over the cross-section. The table gives the maximum of the mean temperature profile measured at $z = 3$ mm. The reported O_2 mass fraction is mass flux-averaged.

Under adiabatic and isobaric circumstances the total (sensible plus chemical) enthalpy is unaffected by chemical reaction, and as such it is a conserved quantity. The heat losses of the coflow bring about an enthalpy deficit: a difference between the adiabatic total enthalpy and the actual total enthalpy. As the enthalpy deficit of the coflow is carried to the flame zone, lower-than-adiabatic flame temperatures (of cold air with cold fuel) are expected. The enthalpy deficit of a stoichiometric mixture of fuel and an oxidiser that consists of flue gases can be expressed as a function of the mixture fraction of the flue gases ξ^0 , the stoichiometric mixture fraction ξ_{st} (both mixture fractions based on the fresh fuel and air streams), and the enthalpy deficit of the oxidiser Δh^0 :

$$\Delta h(\xi_{st}) = \frac{1 - \xi_{st}}{1 - \xi^0} \Delta h^0. \quad (1)$$

Because more heat is lost by radiation of the outer tube when the coflow is hotter, the adiabatic flame temperature is lowest in the DJHC-I case. The adiabatic flame temperatures reported in Table 1 are based on equilibrium chemistry calculations, using the measured coflow properties at $r = 20$ mm.

The fuel used in the central jet was Dutch natural gas which has an approximate composition of 81% methane, 4% ethane, 14% nitrogen and 1% higher alkanes, by volume. Its adiabatic flame temperature in ambient air is 2210 K. Different mass flows were used in the fuel jet, namely 10.7, 16.1 and 30.0 nl/min resulting in jet Reynolds numbers between 2500 and 8800, based on the bulk velocity of the fuel and the density and dynamic viscosity of Dutch natural gas at the estimated fuel temperature at the nozzle exit. These temperatures have been determined using mass conservation, by comparing the measured mass flow and the integrated volume flow at the nozzle exit, from which the density and thus the temperature follows. The reason for taking this approach rather than using the temperature data directly is the quality of the CARS signal obtained close to the fuel pipe exit. Here, the N_2 -CARS spectrum is obscured by the strong non-resonant methane signal. In addition, vibrational CARS suffers from increasing imprecision at lower temperatures.

The jet Reynolds numbers are somewhat limited in magnitude. Though this is generally not advantageous for RANS calculations, it might on the other hand be attractive for LES studies. Measurements were done on a selection of the possible combinations of coflow cases with jet mass flows. The studied combinations are indicated in Table 2, along with their jet Reynolds numbers and fuel temperatures. The higher and lower values of the jet Reynolds number were only fully studied with LDA and CARS in the DJHC-I flames.

The profiles of mean axial velocity of the hot coflow and the fuel jet are shown in Fig. 2. The profiles of temperature and oxygen content are shown in Figs. 3 and 4. The jet Reynolds number does not

Table 1

Characteristics of the coflow stream of the studied DJHC flames. The amount of natural gas to generate the coflow and the total amount of air (premixed and non-premixed) are given in columns two and three. $T_{\text{max;co}}$ is the maximum coflow temperature, whereas $Y_{\text{O}_2;\text{av}}$ is a mass flux weighted average between $r = 2.5$ mm and $r = 35$ mm, at $z = 3$ mm. The subscript “20” denotes properties evaluated at $r = 20$ mm. The mixture fraction ξ_{20}^0 is based on the inlet streams of the burner (normal air and natural gas), whereas $\xi_{st,20}^0$ is the rescaled stoichiometric mixture fraction, of a mixture with the coflow at $r = 20$ mm as oxidiser and natural gas as fuel. The uncertainty of the last digit in the values for enthalpy loss and mixture fraction are given in parentheses.

	Sec. fuel (nl/min)	Tot. air (nl/min)	T_{max} (K)	$Y_{\text{O}_2;\text{av}}$ (–) (%)	Δh_{20}^0 (J/kg)	ξ_{20}^0 (–)	$\xi_{st,20}^0$ (–)	$T_{ad,20}$ (K)
DJHC-I	16.1	224	1540	7.6	$-4.4(5) \times 10^5$	0.052(1)	0.019	1950
DJHC-V	15.3	231	1460	8.8	$-4.0(5) \times 10^5$	0.048(1)	0.024	1980
DJHC-X	14.2	239	1395	10.9	$-2.8(5) \times 10^5$	0.042(1)	0.029	2050

Table 2

Jet Reynolds numbers with fuel temperatures between parentheses, of the combinations of different coflows and jet mass flows that have been fully studied, with both LDA and CARS. For Dutch natural gas, one normal liter corresponds to 0.833×10^{-3} kg. The relative uncertainty in the fuel temperature is estimated at $\pm 5\%$, the uncertainty in the Reynolds numbers is estimated at ± 200 for the $Re = 2500$ and 4100 cases, and ± 300 K for the other cases. The default traverses are at $z = 3, 15, 30, 60, 90, 120$ and 150 mm (radial traverses) and a centerline traverse. The cases superscripted with 1 have a reduced number of measurement locations with the traverses at $z = 15, 30$ and 150 mm and the centerline traverse omitted.

\dot{M}_{jet} (nl/min)	10.7	16.1	30.0
DJHC-I	2500 (470 K) ¹	4100 (430 K)	8800 (360 K)
DJHC-V		4600 (380 K) ¹	
DJHC-X		4600 (380 K)	

influence the oxygen mass fraction nor the temperature significantly at $z = 3$ mm. In both the temperature and oxygen mass fraction profiles, asymmetries are seen that exceed the inaccuracy of the measurements. The maximum difference between the oxygen mass fraction at the left and right side is 0.8%, whereas the left-right deviation of the peak temperature is between 20 and 40 K. With the current design, asymmetries of this magnitude cannot be avoided.

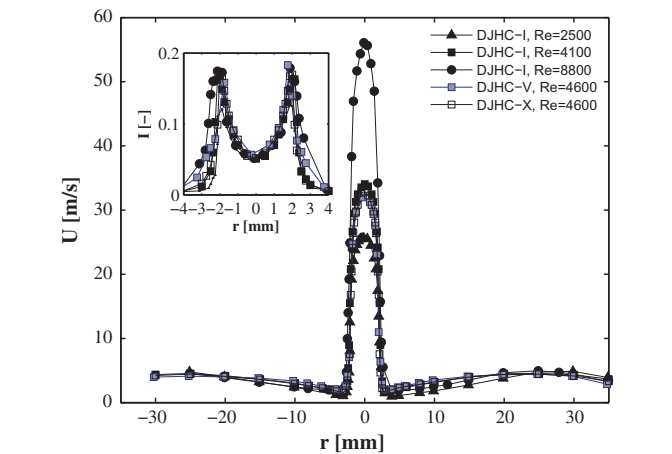


Fig. 2. Axial velocities at $z = 3$ mm, as measured with LDA. The inset shows the turbulence intensity, calculated as $I = (\overline{u'u'} + 2\overline{v'v'})^{1/2} / U_0$, with U_0 the centerline velocity at the nozzle exit.

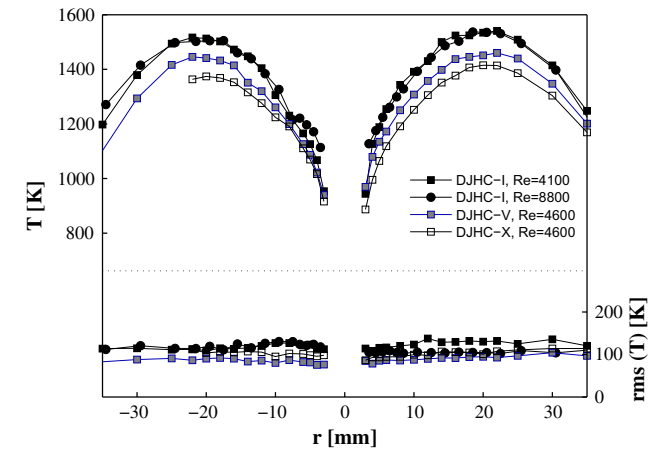


Fig. 3. Mean and RMS of temperature at $z = 3$ mm, measured with CARS.

4. Visual and OH-LIF observations

The visual appearance of several DJHC flames is shown in Fig. 5. As a reference, the bottom right image shows a conventional lifted flame with a jet Reynolds number of 5000 and a coflow velocity of 0.5 m/s. All pictures were taken with identical exposure time, CCD sensitivity and aperture. The jet-in-hot-coflow flames have considerably weaker flame luminescence. In the DJHC-X flame, hardly

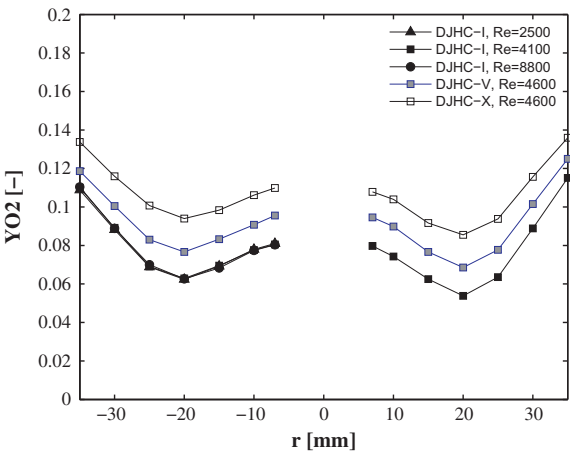


Fig. 4. Oxygen mass fractions at $z = 3$ mm, measured with a flue gas analyser.

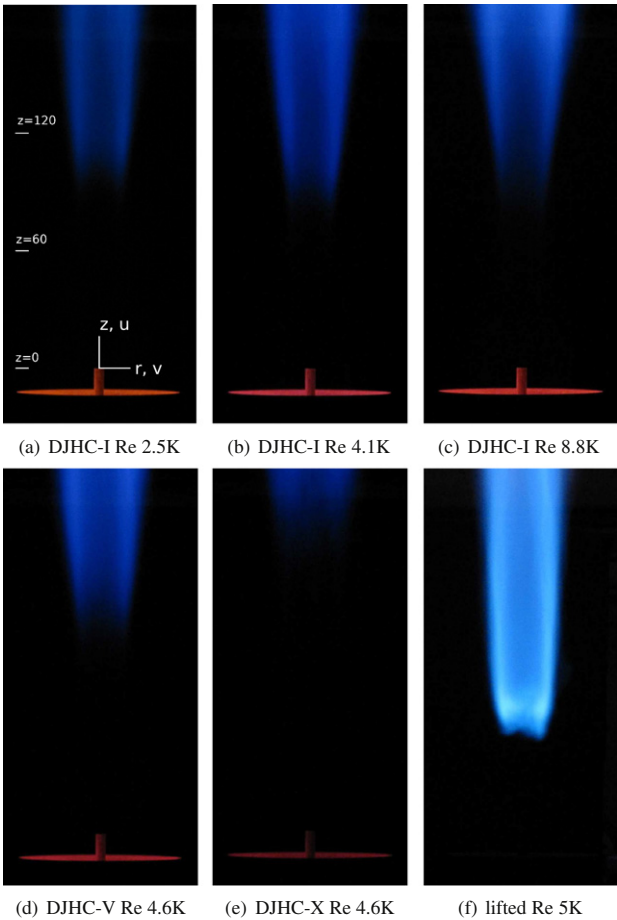


Fig. 5. Images of the DJHC-flames and a conventional lifted flame, all with 0.5 s exposure time and identical aperture. The top of the photograph is in each case at around $z = 180$ mm. The coordinate system is indicated in Fig. 5a.

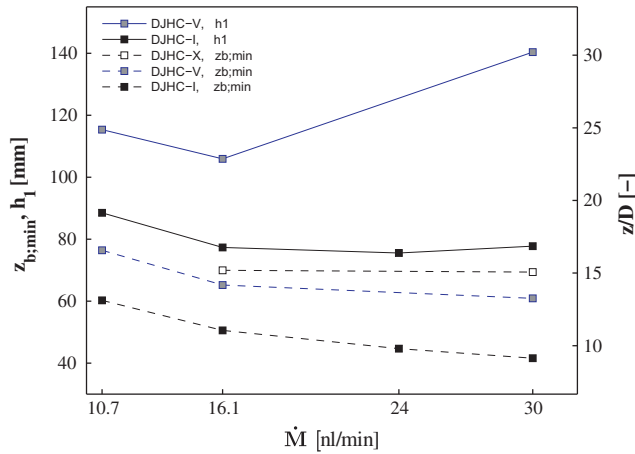


Fig. 6. Lift-off heights (continuous lines) and location of first occurrence of ignition kernels (dotted lines) as a function of the jet mass flow (in nl/min). Note that the flame DJHC-X has a lift-off height exceeding 150 mm in all cases.

any flame luminescence is seen below $z = 150$ mm suggesting that little chemical reactions occur in this region. This is confirmed by OH-PLIF observations, and it makes this flame suitable as a comparison case to the reacting flames.

Figure 6 shows the lift-off heights based on chemiluminescence images obtained with the intensified high-speed camera, with the procedure outlined in [18]. The lift-off heights initially show a decreasing trend as function of the jet Reynolds number. A similar trend can be seen in the Adelaide JHC burner in the cases with 3% oxygen in the coflow [17]. It has been demonstrated that the decrease in lift-off height is related to the lower location of first occurrence of ignition kernels, denoted with $z_{b,min}$ [18]. Both the variation in lift-off height h_1 and $z_{b,min}$ with the jet Reynolds number are shown in Fig. 6. A striking fact is that the initial decrease for all cases is identical. Apparently, the mechanism responsible for lowering the lift-off heights has equal strength in all three coflow cases. It is therefore expected that changes in the flow field are responsible. This aspect will be investigated further in Section 7.

The OH-PLIF images in Fig. 7 were constructed by taking the root mean square (RMS) of the recorded intensities. By taking the RMS value of the OH-PLIF signal, rather than the mean, the occasional appearance of flame pockets at the base of the flame is clearly highlighted. The axial location where flame structures begin to affect significantly the RMS value of the OH signal, decreases by approximately 20 mm from $Re_{jet} = 2500$ to $Re_{jet} = 8800$ in flame DJHC-I. This is consistent with the earlier observations based on

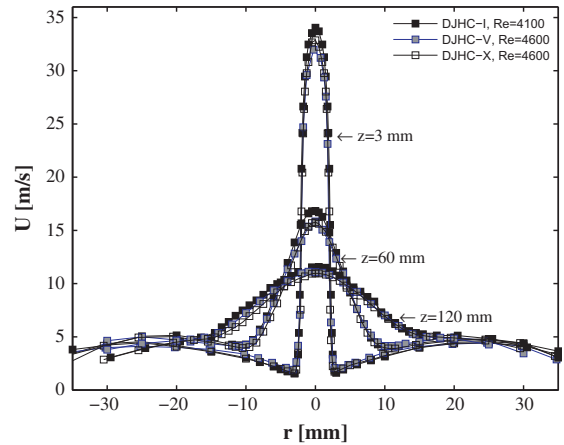


Fig. 8. Mean axial velocities at $z = 3, 60$ and 120 mm for the three different coflow cases, at a jet Reynolds number of 4100 (DJHC-I) and 4600 (DJHC-V and DJHC-X).

flame luminescence regarding the influence of the jet Reynolds number on $z_{b,min}$. The mean OH signal at $z = 90$ mm peaks at a radius of approximately 13 mm for the lowest jet Reynolds number and at approximately 12 mm for the highest jet Reynolds number.

5. Flow field

5.1. Mean velocities and Reynolds stresses

Figure 8 shows the mean axial velocity profiles for the three coflow cases with a jet mass flow of 16.1 nl/min at $z = 3$ mm, 60 mm and 120 mm ($z/d = 2/3, 13 1/3$ and $26 2/3$, respectively). Although flame DJHC-I has a lower lift-off height than flame DJHC-X (observed in both CARS measurements and visually), this is not reflected in a difference in the mean velocity profiles. From this it can be concluded that the effect of combustion on the mean flow-field in the lower portion of the flame is minimal. In Fig. 9, the centerline decay of the mean axial velocity profile (normalised by the jet exit velocity U_0 for two coflow cases and different jet Reynolds numbers) are presented. Whereas the difference in velocity field between the coflow cases is small, there is a clear distinction between the low- and high jet Reynolds number case. The low Reynolds number case shows a weaker initial decay but catches up later, which is also seen in the normalised value of the Reynolds normal stress $\overline{u'u'}$.

The location of maximum shear stress $\overline{u'v'}$ is a useful indicator of the jet width. In the self-similar region of a jet, it peaks at a

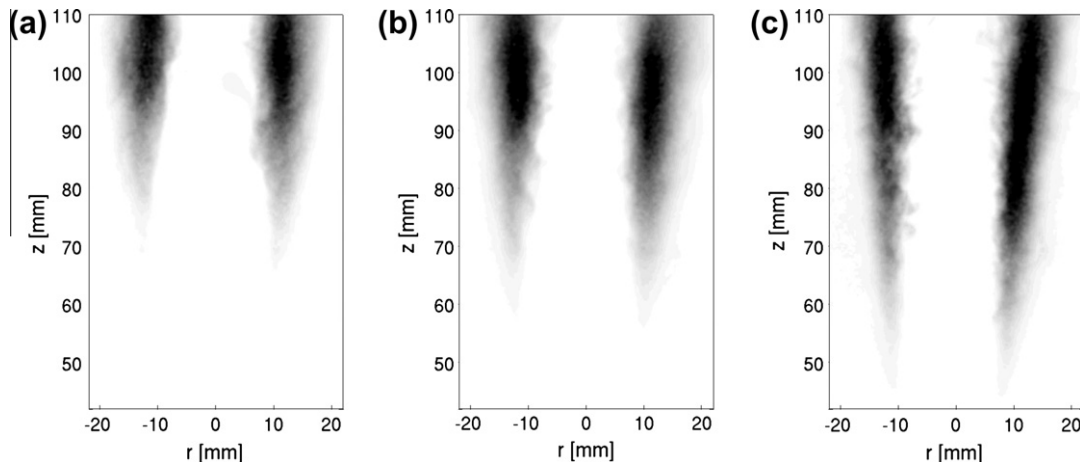


Fig. 7. RMS values of the OH-fluorescence signal in the flame stabilisation region, DJHC-I, $Re_{jet} = 2500$ (a), $Re_{jet} = 4100$ (b) and $Re_{jet} = 8800$ (c).

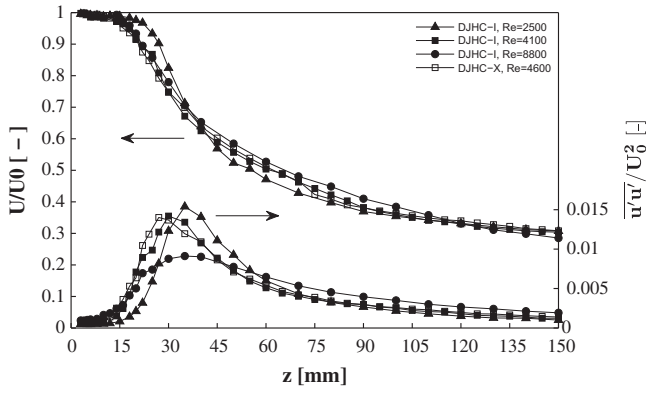


Fig. 9. Centerline decay of the mean axial velocity, all cases.

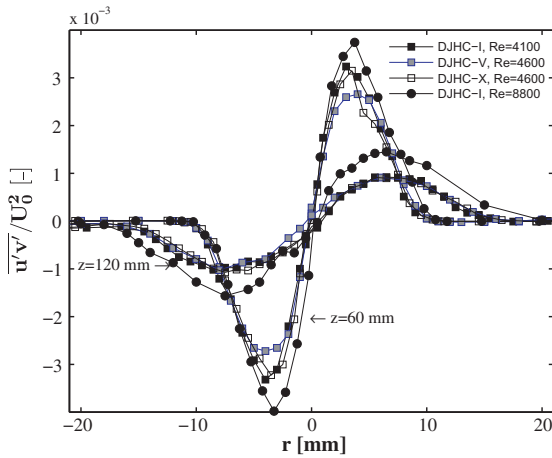


Fig. 10. The shear stress $\overline{u'v'}$ at radial traverses at $z = 60$ and 120 mm, all cases.

radius of roughly 0.7 times the jet half-width (the radius where the mean axial velocity is half that at the centerline) [22]. At $z = 60$ mm and 120 mm, the width of the jet of different cases is very comparable, and the shear stress $\overline{u'v'}$ is of similar magnitude when normalised by the jet exit velocity squared (Fig. 10).

5.2. Turbulence length scales

As turbulence dominates the transport of scalars, an adequate description of the turbulent flow field is important. The Eulerian velocity time scales can be determined from a stationary LDA probe by constructing autocorrelation functions of the velocity components. The turbulence intensity on the jet centerline is sufficiently low ($\sqrt{u'^2}/U \approx 15\%$) to convert these time scales to length scales using Taylor's approximation, as the correction

proposed by Lumley [23] on the Taylor length scale is smaller than 10%. The single point LDA measurements can be used to determine, for instance, integral- and Taylor length scales. The Reynolds number based on the longitudinal Taylor length scale λ_f , $Re_T = \sqrt{u'^2} \lambda_f / \nu$ (with ν the kinematic viscosity) forms a useful quantity to compare experimental and numerical data because it can be determined from numerical data as well (LES or DNS). The longitudinal Taylor length scale follows from the following expansion of the spatial autocorrelation function, as function of the axial separation Δz :

$$\rho(\Delta z) = 1 - \frac{\Delta z^2}{\lambda_f^2} + \mathcal{O}(\Delta z^4), \quad (2)$$

and the transversal Taylor length scale λ_g is defined similarly. These scales are related to the mean square derivatives

$$\left(\frac{\partial u'}{\partial z} \right)^2 = \frac{2\overline{u'^2}}{\lambda_f^2}, \quad \left(\frac{\partial v'}{\partial z} \right)^2 = \frac{2\overline{v'^2}}{\lambda_g^2}. \quad (3)$$

To determine the Taylor-scale Reynolds number, the kinematic viscosity was determined based on equilibrium chemistry calculations (on the centerline, the mixture is still rich and the difference between reacting and non-reacting is minimal). The used kinematic viscosities at $z = 60$ and 120 mm are 8×10^{-5} and $12 \times 10^{-5} \text{ m}^2/\text{s}$, respectively. The integral longitudinal length scale was determined by integration of the longitudinal autocorrelation function.

The properties of the flowfield on the centerline at $z = 60$ and $z = 120$ mm are summarised in Table 3. The transverse Taylor length scale is smaller than the longitudinal length scale. Note that in isotropic turbulence $\lambda_f = \sqrt{2} \lambda_g$ (see [22], p. 199). The Taylor length scale grows with increasing distance from the jet exit along with the integral length scale. The ratio between the Taylor and the integral length scales is not observed to decrease significantly with the jet Reynolds number. Scaling arguments (see for instance [22], p. 200) and measurements (as reported for instance in [24]) suggest an inverse square root relation, but the difference in Reynolds numbers is too small here to be of significance.

To calculate the dissipation of turbulent kinetic energy in general non-isotropic turbulence, twelve different derivative correlations need to be measured, which is practically impossible with single two-component LDA. The assumption of local axisymmetry leads to a relaxation of these demands, but derivatives in the radial directions are still needed [25]. As this direction is not aligned with the mean flow, these derivatives can still not be accessed with a stationary probe. Therefore, to get an estimate of the smallest scales, isotropy of the smallest scales will be assumed. As a measure of the anisotropy, K_1 is also given in Table 3. This quantity is defined as:

$$K_1 = 2 \frac{\overline{\left(\frac{\partial u'}{\partial z} \right)^2}}{\overline{\left(\frac{\partial v'}{\partial z} \right)^2}} \quad (4)$$

Table 3

Turbulence properties on the centerline at two heights above the jet exit, determined with two-component LDA measurements.

Flame	Re	z	U	$\sqrt{u'^2}$	$\sqrt{v'^2}$	λ_f	λ_g	L	Re_λ	K_1	ϵ
	(–)	(mm)	(m/s)	(m/s)	(m/s)	(10^{-3} m)	(10^{-3} m)	(10^{-3} m)	(–)	(–)	($10^3 \text{ m}^2 \text{ s}^{-3}$)
DJHC-I	4100	60	16.2	2.8	2.2	1.9[±0.3]	1.3[±0.2]	2.6	7×10^1	1.5	5
	4100	120	10.9	1.5	1.3	3.4[±0.1]	2.3[±0.1]	5.0	5×10^1	1.3	0.7
	8800	60	30.4	5.1	4.1	1.4[±0.1]	1.1[±0.1]	2.1	9×10^1	1.7	30
	8800	120	20.1	3.2	2.7	2.4[±0.3]	1.6[±0.1]	3.9	7×10^1	1.2	6
Lifted	5000	60	6.6	1.5	1.2	1.3[±0.4]	1.0[±0.3]	2.9		1.9	
	5000	120	4.0	0.6	0.5	2.8[±0.1]	1.7[±0.1]	5.3		1.2	

and it is equal to one in isotropic conditions [25]. As can be seen in the table, the deviations from unity are not large at $z = 120$ mm. An estimate of the dissipation rate of turbulent kinetic energy based on the expression for isotropic turbulence ($\epsilon = 30\nu u'^2/\lambda_f^2$) is included in the final column. The Kolmogorov length-scale $\lambda_K = (\nu^3\epsilon^{-1})^{1/4}$ is in the order of 1×10^{-4} m.

6. Temperature field

The high-speed intensified imaging reported in [18] described the probability of the presence of flame structures as a function of axial height, for various flames. This probability was expressed in the parameter denoted with P_{b1} . This parameter will be used in this section for comparison, a discussion on its definition is provided in the aforementioned paper. The temperature measurements at $z = 60$ mm (not shown) show no sign of any reactions. On the other hand, at $z = 90$ mm a mild temperature increase can be observed in the DJHC-I flame, see Fig. 11. This increase is hardly noticeable in the mean, but is visible in the temperature RMS, and, most notably, in the peak temperature T_{99} . This peak temperature is defined as the temperature where the cumulative density function exceeds 99% (it is the 99th percentile). Although flame structures are present during approximately 80% of the time at $z = 90$ mm ($P_{b1} \approx 80\%$), the peak temperature T_{99} does not exceed 1770 K, relatively far from the estimated adiabatic flame temperature of 1950 K. Comparing the locations of the peaks in T_{99} in Fig. 11 (at a radial location of around 12 mm, which is in agreement with the location of the flame as observed in the OH-PLIF measurements) with the measured shear stress profile at $z = 90$ mm (which peaks at a radius of 5 mm), the reaction zone clearly resides outside the region of most intense turbulence. This can be understood from the value of the stoichiometric mixture fraction, being even lower than that of a flame of Dutch natural gas in air (around 0.02 instead of 0.07) due to the reduced oxygen content of the coflow.

At $z = 120$ mm, the presence of the reaction zone of flame DJHC-I is visible in the mean temperature profile, whereas this is less clear in flame DJHC-V, see Fig. 12. An interesting feature is that T_{99} of flame DJHC-I, increases by some 140 K from $z = 90$ to $z = 120$ mm, to around 1910 K. As the flame probability P_{b1} is already close to 100% at $z = 90$ mm, this increase must be due to an evolution of the flame temperature. Taking into account the convective velocity of the flame pockets, which is roughly 5 m/s [18], the flame pockets have a lifetime that is around 6 ms longer

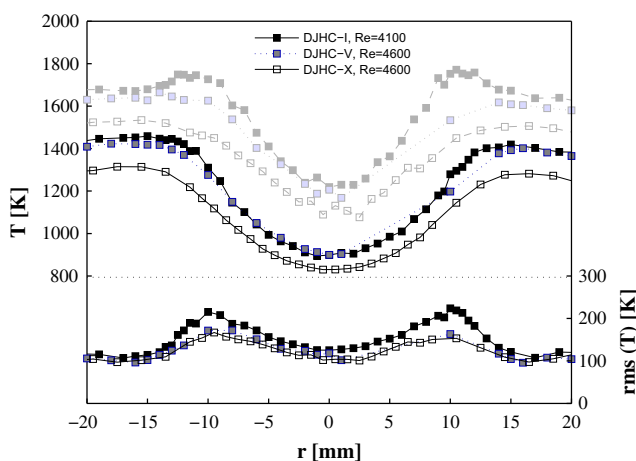


Fig. 11. Mean and RMS of temperature in flames DJHC-I, DJHC-V and DJHC-X at $z = 90$ mm. The fainter upper curves indicate T_{99} , the 99 percentile of temperature, to indicate measured peak temperatures.

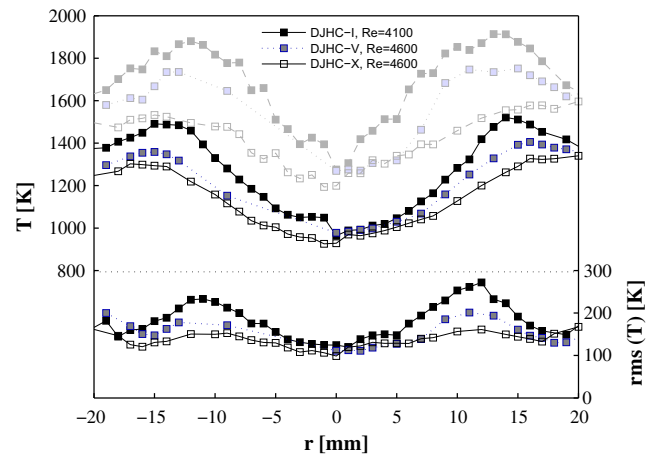


Fig. 12. Mean and RMS of temperature in flames DJHC-I, DJHC-V and DJHC-X at $z = 120$ mm. The fainter upper curves indicate T_{99} , the 99 percentile of temperature.

at $z = 120$ mm than at $z = 90$ mm. Apparently, this time is needed for the flame pockets to reach temperatures close to equilibrium.

The DJHC-V flame does not, despite its higher adiabatic flame temperature, show higher mean or peak temperatures at $z = 120$ than DJHC-I. Flame structures are also present regularly here ($P_{b1} \approx 65\%$), another indication that chemistry resides far from equilibrium.

As a reference, temperature statistics were also obtained for a conventional lifted flame with a jet Reynolds number of 5000, at a height of $z = 90$ mm (which is above the lift-off height) and at the radial location with the highest mean temperature ($r = 15$ mm). The pdf of temperature of this flame is shown together with that of the DJHC-I flame in Fig. 13. The peak temperature T_{99} of the lifted flame (indicated with the right dotted line) is 2100 K. When rescaled between the mixing temperature and the adiabatic flame temperature, this is comparable to the T_{99} of DJHC-I at $z = 120$ mm. The temperature distribution of the lifted flame is much wider, containing both colder samples as the reactants are injected at room temperature, and much hotter samples. Figure 14 compares the temperatures at $z = 90$ mm for varying jet Reynolds numbers. Only minor differences can be spotted. The mean temperatures vary insignificantly, the T_{99} values of the

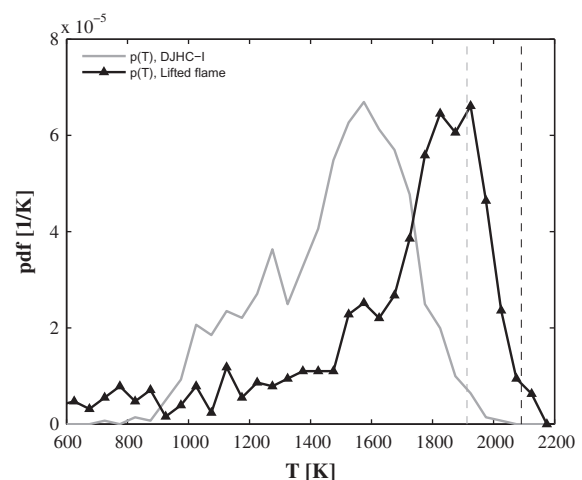


Fig. 13. Pdf of temperature $p(T)$ (points lie on the center of the bins) for the DJHC-I flame ($Re_{jet} = 4100$, at $z = 120$ mm, $r = 14$ mm) and a lifted flame ($Re_{jet} = 5000$ at $z = 90$ mm, $r = 15$ mm), the vertical dashed lines denote the T_{99} values. The number of measurements is 951 (DJHC-I) and 772 (lifted flame).

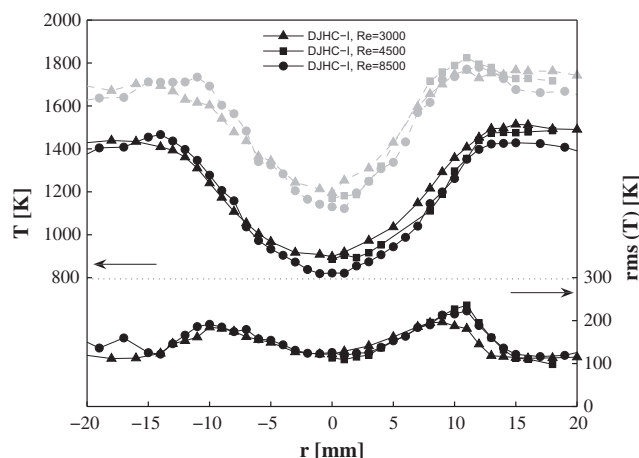


Fig. 14. Mean and RMS of temperature for three jet Reynolds numbers in flame DJHC-I, $z = 90$ mm. The fainter upper curves indicate T_{99} .

lowest jet Reynolds number case are slightly lower, in agreement with its higher lift-off. In the highest jet Reynolds number case, colder temperatures were occasionally measured at $r = -17$ mm (2% of the samples were below 1000 K), originating from the ambient air. These are responsible for the increase in the RMS values.

The differences are more substantial at $z = 120$ mm. Figure 15 shows that the mean temperatures as well as the peak temperatures are substantially lower in the higher Reynolds number case. The mean temperatures in this case are even lower than those at $z = 90$ mm, which can only be explained by the entrainment of colder coflow air. A stronger departure from chemical equilibrium due to shorter residence time of flame pockets, and possibly the influence of larger strains could form an additional explanation for the fact that the peak temperatures do not exceed those at $z = 90$ mm significantly, as they do in the lower Reynolds number cases. As the influence of ambient air (witnessed as outliers in the pdfs of temperatures) is present from $r = 12$ mm and up in the high jet Reynolds number case (in the other cases at $r = 20$ mm and up), it is difficult to be conclusive regarding this point.

7. Entrainment

A remarkable feature of the studied flames is that ignition events are first observed at lower heights with increasing jet

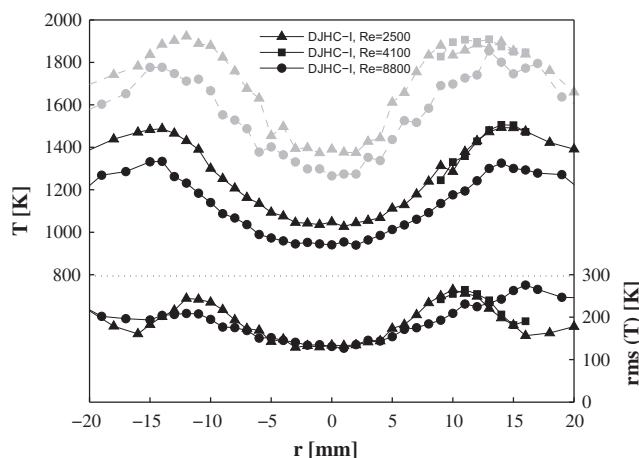


Fig. 15. Mean and RMS of temperature for three jet Reynolds numbers in flame DJHC-I, $z = 120$ mm. The fainter upper curves indicate again T_{99} .

Reynolds number. An explanation for this phenomenon will be provided in this section. Of interest to this problem are the properties in the mixing layer, located radially somewhere between the jet centerline and the pure coflow fluid outside the jet. Here, mixtures of fuel and coflow fluid with the optimum mixture fraction for fast ignition are formed (in general not equal to the stoichiometric mixture fraction, [26]). The total mass flow in the jet increases in the downstream direction, as more and more coflow fluid is drawn into the jet. Because of this continuous increase in mass flow, the coflow fluid that is entrained by the jet originates from progressively larger radii at $z = 0$ as one goes downstream. If the properties of the coflow are non-constant along the radial direction, the properties of the entrained coflow fluid will then also change in the downstream direction. For the DJHC flames, this means that the fuel stream initially mixes with the colder coflow fluid, originating from small radii at $z = 0$. As more coflow fluid is consumed by the jet, the hotter coflow from larger radii will find its way into the mixing layer at larger heights. The temperature conditional on (the most reactive) mixture fraction will increase in the axial direction and ignition delay times will become sufficiently short for ignition kernels to form in the domain. In this analysis, it is assumed that the temperature of a parcel of coflow fluid as it is entrained is related to the temperature of that fluid parcel when it was at $z = 0$. This is justified by a simple scaling argument: the convective heat flux is much stronger than the diffusive heat flux ($\tilde{u}T \gg u''T''$), since turbulent fluctuations are relatively small in the coflow. Because the length scales for convection (length of streamline) and diffusion (radius of the burner tube) are of similar magnitude, the time scale for turbulent diffusion is much greater than the timescale for convection. As a consequence, temperatures are largely conserved along streamlines in the coflow.

Since the entrainment flux of turbulent jets is proportional to the centerline velocity (see [27], p. 35), this transport of hotter coflow fluid from larger radii at $z = 0$ toward the jet is augmented when the jet velocity is increased. In the presence of a positive radial temperature gradient of the coflow this results in a faster rise of temperatures conditional on mixture fraction in the axial direction, with ignition at lower axial locations as a result. Note that in this analysis, two important assumptions were made. First of all, details of the mixing process itself are not considered. This is not to say that these complexities (such as the influence of scalar gradients on the mixing and ignition process [28]) are not present, but rather that their influence is overshadowed by the effect of the temperature variations. Secondly, ignition delay times are transformed to ignition delay lengths using a constant velocity, independent of the jet velocity. This assumption is justified by the experimental finding that the convective velocity of ignition kernels is not strongly affected by the jet velocity, but is mainly determined by the coflow velocity [18].

The transport of coflow fluid toward the mixing region in the jet can be studied quantitatively with the available temperature and velocity data. The task is to find the radial position r' at $z = z_0$ from which the streamline that is entrained at (r', z') originates, see Fig. 16. By definition the mass flow rate through any boundary that runs from a point p to any point q on a streamline S is constant, independent of the choice of q . If the value of the streamfunction Ψ is set to zero at (r_0, z_0) , the streamline $S(\Psi)$ in Fig. 16 connects points q' and q^* for which $\dot{M}_c = \dot{M}_e = \Psi$.

Now, a criterion is needed to define the interface between the turbulent mixing layer and the coflow stream. This criterion is provided by the turbulent shear stress $\overline{u''v''}$. As demonstrated in Fig. 10, the value of this shear stress at $z = 60$ mm quickly approaches zero at the jet edge, enabling the use of a stringent threshold level. The edge of the jet is defined as the radius r^* where $\overline{u''v''}$ is less than 1% of its peak value.

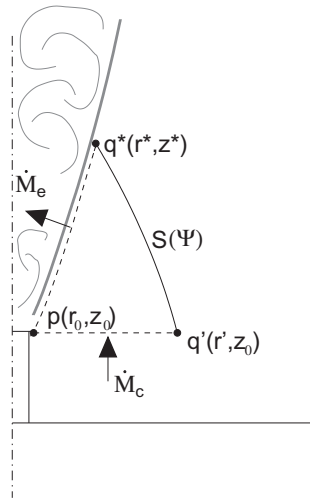


Fig. 16. Sketch of the jet boundary (curved thick line) and the streamline S . In absence of circulation regions, points q' and q^* share the same streamline S , when the mass flow through the boundary $p-q^*$ (which is the total entrained coflow fluid by the jet between z_0 and z^*) equals the mass flow through the boundary $p-q'$. The thick grey line denotes the boundary between the jet region, where jet and coflow fluid mix, and the coflow region.

The value of the entrainment mass flow, \dot{M}_e , can be obtained by integration along the jet boundary, as was done by Han and Mungal [29]. This requires a careful determination of the angle of the jet boundary, and calculation of the mass flow perpendicular to this boundary. A different approach is taken here, using a control volume that runs from (r_0, z_0) via (r^*, z_0) to (r^*, z^*) . The entrained mass flow between $z = z_0$ and $z = z^*$ is the sum of two integrals, one in radial and one in axial direction:

$$\dot{M}_e(z^*) = 2\pi \left[\int_{r_0}^{r^*} \bar{\rho} u r dr \Big|_{z_0} + \int_{z_0}^{z^*} -\bar{\rho} v r dz \Big|_{r^*} \right]. \quad (5)$$

See Fig. 16 for a definition of the coordinates r_0 , r^* , z_0 and z^* . The mass flows in Eq. (5) are not measured directly. Whether and how these can be reconstructed from the CARS and LDA measurements, depends on the nature of the averages of these measurements. Since the timing of CARS measurements is controlled externally, and the data is gathered independently of processes in the flame, the temperature measurements can be considered to be unconditionally sampled. If temperature variations within the measurement volume can be neglected, the arithmetic mean of CARS measurements therefore corresponds to a Reynolds average. For LDA measurements the analysis is more complicated. In Appendix A it is shown that LDA statistics obtained in a variable density flow with application of transit time weighting can be considered to be density weighted. Multiplication of this density weighted mean velocity by the mean density then gives the mean mass flux, as required to calculate Eq. (5), since by definition $\bar{\rho} \bar{u} = \overline{\rho u}$.

This point is not of critical importance, since the fluctuations of density are small. To illustrate this, consider the maximum value of the covariance given by the Cauchy–Schwarz inequality:

$$|\overline{\rho' v'}| \leq (\overline{\rho'^2} \overline{v'^2})^{1/2}. \quad (6)$$

The density variance can be approximated from the temperature variance using a linearised relation between density and temperature around the mean temperature:

$$\overline{\rho'^2} \approx \left. \frac{d\rho}{dT} \right|_{\bar{T}}^2 \overline{T'^2}. \quad (7)$$

If the measured velocities would in fact be Reynolds averaged, the uncertainty (as in principle, the correlation can have any value between one and minus one) is typically 10% or smaller.

Approximating the functions in the integrals of Eq. (5) linearly between the measurement points, the total entrainment can be calculated. The totally entrained mass flow at several heights is shown in Fig. 17. The entrainment of cases DJHC-I and DJHC-X with a jet mass flow of 16.1 nl/min is identical. Furthermore, the higher velocity jet entrains more coflow fluid, as can be expected from a standard entrainment scaling [27]. The data shown in Fig. 17 can now be used to estimate the average temperature of the coflow entrained by the jet at different heights.

The values of $T(r)$ as a function of $\Psi_0(r)$, where Ψ_0 is the value of \dot{M}_c at $z = 3$ mm, are plotted in Fig. 18. The coflow temperature levels off at around $\Psi_0 = 0.6 \times 10^{-3}$ kg/s, corresponding to $r \approx 15$ mm. The temperature profile is much flatter against Ψ than against r , because the majority of the coflow mass flows through the center and outer part of the annulus.

Comparing now Fig. 17 with Fig. 18, it can be seen that at $z = 30$ mm, the highest jet Reynolds number case starts entraining the hottest part of the coflow (at around 1500 K), whereas this happens at around 20 mm further downstream for the lowest jet Reynolds number case. This magnitude is in agreement with that of the observed decrease in the height where ignition kernels are first formed. The combination of the dependence of the entrainment

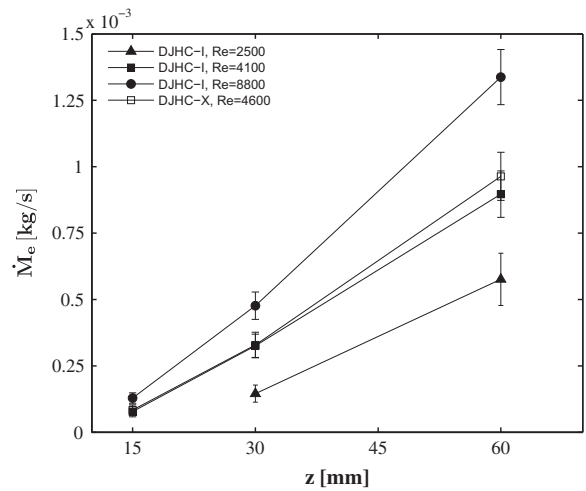


Fig. 17. The total entrainment \dot{M}_e , determined by numerical evaluation of Eq. (5), as a function of height z , for four different cases. The errorbars indicate the maximum contribution of the density–velocity covariance calculated with Eq. (6).

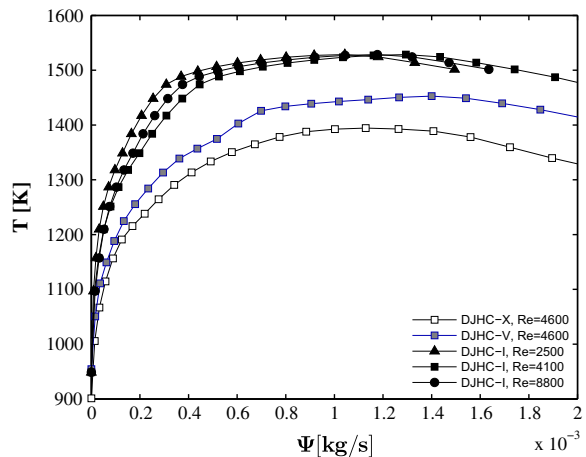


Fig. 18. Mean temperature as a function of the streamfunction Ψ (set to zero at $r = 3$ mm), at $z = 3$ mm.

fluxes on the jet velocity with the positive radial temperature gradient of the coflow therefore forms a sound explanation for the observed initial decrease in lift-off height.

8. Conclusions

LDA, CARS and OH-PLIF measurements were performed in several jet-in-hot-coflow flames, differing in jet mass flow and coflow temperature. The chemical reactions occurring in these flames were found to have a very weak impact on the velocity field, as the mean velocities and turbulent stresses in the DJHC-I flame are comparable to those of the DJHC-X case, that has a lift-off height exceeding the measurement domain.

In the temperature field, first deviations between the reacting and non-reacting cases were seen at $z = 90$ mm. These differences are not very pronounced in the mean, but are evident both in the RMS values (nearly doubling when reactions start to occur, case DJHC-I vs. DJHC-X), and in the 99 percentile of temperature, T_{99} . The peak temperatures in the DJHC-I, $Re_{jet} = 4100$ case at $z = 90$ mm are far away from the adiabatic peak temperature whereas those at 120 mm approach this temperature much closer. Considering the fact that flame structures are already present most of the time at a height of 90 mm, this is indicative of an evolution in temperature of flame pockets from the point where they are newly formed to where they have evolved longer in time (a difference in time of around 6 ms). In other flames (DJHC-I with $Re_{jet} = 8800$ and the colder coflow flame DJHC-V with $Re_{jet} = 4600$), peak temperatures stay remote from the adiabatic flame temperatures, also at $z = 120$ mm.

It was observed with both high-speed flame luminescence and OH-PLIF measurements that the location of first chemical reactions decreases with increasing jet velocity. This is by no means a general characteristic of jet-in-hot-coflow flames, but is related to the positive radial temperature gradient in the coflow of the DJHC-burner. From a quantitative analysis of the entrainment in the near-nozzle region, it was concluded that the hottest part of the coflow finds its way into the jet shear layer at an axial location that is around 20 mm lower going from the lowest to the highest jet values of the jet mass flow. This distance agrees with the observed decrease. The rate with which hot oxidizer fluid is transported towards the edge of the jet where mixing takes place is thus an important factor in the flame stabilisation of the flames considered. This result is in line with the dominant role of autoignition in the stabilisation of jet-in-hot coflow flames and the known sensitivity of autoignition processes to temperature.

In the $Re_{jet} = 8800$ case, at $z = 120$ mm, cold outer air is occasionally entrained in the location where the flame resides as seen by outliers in the temperature pdf's, highlighting the necessity of using a larger diameter coflow when larger jet Reynolds numbers or higher locations are to be studied.

Appendix A. Density weighted nature of transit-time corrected LDA data

Several sources of statistical biasing in LDA data have been recognised, most notably those related to the velocity itself [30]. In flows with varying density, another bias will arise. Intuitively, one can see that a fluid parcel with low fluid density will have a low seeding density and thus a lower probability of detection by the LDA system. Therefore, one might expect the velocity statistics to be affected by these density fluctuations. Goss et al. [31] showed that in their combined CARS/LDA setup, the temperature pdf's, conditional on the presence of a simultaneous LDA measurement (presence of a seeding particle), were very similar to density weighted CARS measurements. In [32], combined LDA and CARS

measurements were carried out to investigate velocity–temperature correlations, using the LDA measurements to compute Favre averaged quantities. Nevertheless, not much attention has been given in literature how LDA data in a variable density environment should be interpreted.

The bias in LDA measurements occurs because the data rate \dot{n} (expected number of seeding particles passing through the measurement volume per time) is a function of the value of the instantaneous velocity vector \underline{U} , and possibly of other properties such as the density ρ . The joint pdf of the measured velocity vector, $f_{\underline{U};LDA}$ is a function of the original pdf of velocity and the conditional data rate:

$$f_{\underline{U};LDA} = f_{\underline{U}} \frac{\langle \dot{n} | \underline{V} \rangle}{\langle \dot{n} \rangle}, \quad (A.1)$$

with the averaging operator defined as:

$$\langle \cdot \rangle = \int_{\psi} \int_{\underline{V}} \cdot f_{\underline{U}\rho} d\underline{V} d\psi. \quad (A.2)$$

\underline{V} and ψ form the sample space of the variables \underline{U} and ρ , respectively. The instantaneous data rate is equal to

$$\dot{n} = \rho c_m \dot{V}, \quad (A.3)$$

with \dot{V} the volume flux and c_m the seeding density, [–/kg] [33]. To eliminate the bias, some kind of correction is necessary. This is realised in practice by applying an appropriate weighting factor w to the data points. To demonstrate the connection between application of weighting factors on data points and the scaling of the pdf, consider the variable \underline{U} that has a pdf $f_{\underline{U}}$ and is weighted with weight factors w to yield the weighted pdf $f_{\underline{U};w}$:

$$\begin{aligned} f_{\underline{U};w}(V_k) &= \lim_{N \rightarrow \infty} \lim_{\Delta u \downarrow 0} \sum_{m=1}^M w_{m,k} \left(\Delta u \sum_{m=1}^N w_{m,k} \right)^{-1} \\ &= f_{\underline{U}}(V_k) \frac{\langle w | V_k \rangle}{\langle w \rangle}, \end{aligned} \quad (A.4)$$

Here, N is the total number of data points, and M the number of datapoints between $V_k - \frac{1}{2}\Delta u$ and $V_k + \frac{1}{2}\Delta u$. Therefore, if the conditional expectation of the weight factor is inversely proportional to the conditional data rate $\langle \dot{n} | \underline{V} \rangle$, application of this weight factor on Eq. (A.1) will result in unbiased statistics, since the measured pdf after correction is:

$$f_{\underline{U};LDA^c} = f_{\underline{U}} \frac{\langle \dot{n} | \underline{V} \rangle \langle w | \underline{V} \rangle}{\langle \dot{n} w \rangle}, \quad (A.5)$$

Hoesel and Rodi [33] found that, in a constant density flow, the transit time satisfies this criterion. The transit time is a random variable for a given value of \underline{V} (seeding particles pass the measurement volume at arbitrary locations), with expectation :

$$\langle tr | \underline{V} \rangle = \frac{V_p}{\dot{V}(\underline{V})} = \frac{V_p \rho c_m}{\dot{n}(\underline{V})} \propto \frac{\rho}{\dot{n}(\underline{V})}, \quad (A.6)$$

with V_p the probe volume (which is independent of the flow direction, see the Appendix in [33] for a discussion). The LDA data reported in this study has also been transit-time weighted to avoid the velocity bias. In absence of density fluctuations, unbiased estimates for mean velocities and (co)variances can now be obtained by weighting each measurement with its individual transit time tr_i .

When density fluctuations do occur, the pdf of the measured velocities after weighting is (using $\langle \dot{n} | \underline{V} \rangle = \langle \rho | \underline{V} \rangle c_m \dot{V}(\underline{V})$ and Eq. (A.5)):

$$f_{\underline{U};LDA^c} = f_{\underline{U}} \frac{\langle \rho | \underline{V} \rangle c_m \dot{V}(\underline{V}) \dot{V}^{-1}(\underline{V})}{\langle \rho \rangle c_m} = f_{\underline{U}} \frac{\langle \rho | \underline{V} \rangle}{\langle \rho \rangle}, \quad (A.7)$$

which is the Favre pdf. Therefore, if transit time corrections are applied to LDA data obtained in a flow with uniform seeding density per mass (which is in principle not influenced by thermal expansion due to combustion), density weighted quantities will be obtained, i.e.:

$$\sum_{i=1}^N u_i tr_i / \sum_{i=1}^N tr_i = \frac{\overline{\rho u}}{\bar{\rho}},$$

$$\sum_{i=1}^N u_i v_i tr_i / \sum_{i=1}^N tr_i = \frac{\overline{\rho u v}}{\bar{\rho}}, \quad \text{etc.}$$

References

- [1] J.A. Wüning, J.G. Wüning, *Prog. Energy Combust. Sci.* 23 (1) (1997) 81–94.
- [2] M. Flamme, *Appl. Therm. Eng.* 24 (11–12) (2004) 1551–1559.
- [3] C.T. Bowman, *Proc. Combust. Inst.* 24 (1992) 859–878.
- [4] R.S. Barlow, *Proc. Combust. Inst.* 31 (2007) 49–75.
- [5] C. Galletti, A. Parente, L. Tognotti, *Combust. Flame* 151 (4) (2007) 649–664.
- [6] M. Mancini, P. Schwoppe, R. Weber, S. Orsino, *Combust. Flame* 150 (1–2) (2007) 54–59.
- [7] M. Mortberg, W. Blasiak, A.K. Gupta, *Combust. Sci. Technol.* 178 (7) (2006) 1345–1372.
- [8] S. Orsino, R. Weber, *Combust. Sci. Technol.* 170 (2001) 1–34.
- [9] K.N.C. Bray, *Proc. Combust. Inst.* 26 (1996) 1–26.
- [10] R. Cabra, T. Myhrvold, J.Y. Chen, R.W. Dibble, A.N. Karpetis, R.S. Barlow, *Proc. Combust. Inst.* 29 (2002) 1881–1888.
- [11] B.B. Dally, A.N. Karpetis, R.S. Barlow, *Proc. Combust. Inst.* 29 (2002) 1147–1154.
- [12] R. Cabra, J.Y. Chen, R.W. Dibble, A.N. Karpetis, R.S. Barlow, *Combust. Flame* 143 (4) (2005) 491–506.
- [13] R. Cabra, R. Dibble, Berkeley VCB CH4/air site. <<http://www.me.berkeley.edu/cal/vcb/data/VCMAData.html>>.
- [14] R. Cabra, R. Dibble, Berkeley VCB H2/N2 site. <<http://www.me.berkeley.edu/cal/vcb/data/VCHNData.html>>.
- [15] Z.J. Wu, A.R. Masri, R.W. Bilger, *Flow Turbul. Combust.* 76 (1) (2006) 61–81.
- [16] R.L. Gordon, A.R. Masri, E. Mastorakos, *Combust. Flame* 155 (2008) 181–195.
- [17] P.R. Medwell, P.A.M. Kalt, B.B. Dally, *Combust. Flame* 148 (1–2) (2007) 48–61.
- [18] E. Oldenhof, M. Tummers, E. van Veen, D. Roekaerts, *Combust. Flame* 157 (6) (2010) 1167–1178.
- [19] M. Tummers, D. Passchier, *Meas. Sci. Technol.* 12 (2001) 1641–1650.
- [20] E.H. Van Veen, D. Roekaerts, *Combust. Sci. Technol.* 175 (10) (2003) 1893–1914.
- [21] J. Warnatz, U. Maas, R. Dibble, *Combustion – Physical and Chemical Fundamentals, Modelling and Simulation, Experiments, Pollutant Formation*, Springer-Verlag GmbH, 2006.
- [22] S.B. Pope, *Turbulent Flows*, Cambridge University Press, 2000.
- [23] J.L. Lumley, *Phys. Fluids* 8 (6) (1965) 1056–1062.
- [24] H. Fellouah, A. Pollard, *Phys. Fluids* 21 (11) (2009) 115101.
- [25] W.K. George, H.J. Hussein, *J. Fluid Mech.* 233 (1991) 1–23.
- [26] A. Liñán, A. Crespo, *Combust. Sci. Technol.* 14 (1–3) (1976) 95–117.
- [27] N. Rajaratnam, *Turbulent Jets*, Elsevier Scientific publishing company, Amsterdam, 1976.
- [28] E. Mastorakos, *Prog. Energy Combust. Sci.* 35 (1) (2009) 57–97.
- [29] D.H. Han, M.G. Mungal, *Combust. Flame* 124 (3) (2001) 370–386.
- [30] D. McLaughlin, W. Tiederman, *Phys. Fluids* 16 (12) (1973) 2082–2088.
- [31] L.P. Goss, D.D. Trump, W.M. Roquemore, *Exp. Fluids* 6 (3) (1988) 189–198.
- [32] M.J. Tummers, E.H. van Veen, N. George, R. Rodink, K. Hanjalic, *Exp. Fluids* 37 (3) (2004) 364–374.
- [33] W. Hoesel, W. Rodi, *Rev. Sci. Instrum.* 48 (7) (1977) 910–919.